A TIME-EFFICIENT, DATA DRIVEN MODELLING APPROACH TO PREDICT THE GEOMAGNETIC IMPACT OF CORONAL MASS EJECTIONS

Souvik Roy[1], **Dibyendu Nandy**[1,2]

[1]Center of Excellence in Space Sciences India, Indian Institute of Science Education and Research Kolkata, Mohanpur 741246, India

[2]Department of Physical Sciences, Indian Institute of Science Education and Research Kolkata, Mohanpur 741246, India

Key Points:

- We present a new data driven modelling framework for timely predictions of the geoeffectiveness of solar magnetic storms.
- Our magnetohydrodynamic model reproduces well the timing and intensities of a strong and a moderate geomagnetic storm.
- Our work identifies causal pathways of solar storm magnetospheric interactions that can lead to operational space weather forecasts.

Corresponding author: Dibyendu Nandy, `dnandi@iiserkol.ac.in`

Abstract

Coronal mass ejections (CMEs) are transient solar eruptions of magnetised plasma from the Sun's corona. Their interactions with the geo-magnetosphere may lead to severe geomagnetic perturbations. Such space weather events pose a threat to ground- and space-based technologies thereby impacting modern societal infrastructure. To understand the physical processes behind geomagnetic storms and predict them we develop a new CME flux rope-magnetosphere interaction module using 3D magnetohydrodynamics. Our approach is relatively simpler and time-efficient compared to more complex models but performs well in estimating the strength and temporal variations of geomagnetic storms. Simulated postdictions for two contrasting coronal mass ejections from 2003 and 2006 exhibit strong linear correlation with observed Dst and SYM-H indices. This study paves the way for operationally efficient prediction of CME flux rope driven geomagnetic storms.

Plain Language Summary

Space weather refers to variations in the near-Earth space environment and atmosphere in response to magnetic activity of the Sun. Extreme space weather events have the potential to damage space- and ground-based technologies. With increasing dependence on space-reliant technologies such as communication, navigational networks and interconnected power grids, human societies have become more susceptible to space weather disruptions. Energetic solar magnetic storms known as Coronal Mass Ejections (CMEs) are responsible for the most severe perturbations to the geomagnetic environment. Development of physics-based models to predict the strength and timing of geomagnetic storms are therefore of critical importance. Based on a new, data driven magnetohydrodynamic modeling approach – the CESSI-Storm Interaction (STORMI) Module – we develop a methodology to predict the timing and intensity of CME driven geomagnetic storms. We successfully demonstrate the efficacy of this modeling framework in predicting the geomagnetic consequences of solar storms in a computationally efficient manner that is suitable for operational forecasts.

1 Introduction

Dynamic magnetic conditions on the Sun are known to regulate the near-Earth space environment giving rise to space weather. The primary drivers of such disturbances are coronal mass ejections (CMEs), which are expulsions of plasma embedded in magnetic fields from the solar outer atmosphere. Such large-scale solar eruptions originate due to magnetic reconnection, instabilities and rapid restructuring of coronal magnetic field driven by surface flux emergence and evolution (Gopalswamy, 2004; Yeates et al., 2010; Sinha et al., 2019). On their arrival at Earth, their interplanetary counterparts, ICMEs (Burlaga et al., 1982; Gosling, 1990; Gopalswamy, 2002, 2006b; Gopalswamy et al., 2006), drive geomagnetic storms which can have significant impact on ground and space based technologies (Y. D. Liu et al., 2014; Schrijver, 2015; Schrijver et al., 2015; Nandy et al., 2021). As we approach the next solar maximum (Bhowmik & Nandy, 2018; Nandy, 2021), we expect to see a rise in the number of such extreme events (Lakhina & Tsurutani, 2016; Love, 2021).

The intensity of a geomagnetic storm (geoeffectiveness) is quantified using different geomagnetic indices. Of these, the most commonly used are the Disturbance Storm Time Index (Dst, Kyoto Dst) (Sugiura & Kamei, 1991) and its high-resolution twin, SYM-H index (Iyemori et al., 2009). These indices measure the storm-associated changes in the magnitude of the axially symmetric component of the geomagnetic field using various ground-based observatories (Gonzalez et al., 1994; Wanliss & Showalter, 2006; Menvielle et al., 2011). For the purpose of space weather forecasting, various analytical and computational schemes have been employed to predict Dst (Rastätter et al., 2013). Some widely used popular approaches in this context are the Space Weather Modelling Framework (SWMF) (Tóth et al., 2005; Ngwira et al., 2014; M. Liemohn et al., 2018; Welling et al., 2021), the Open Geospace General Circulation Model (Open GGCM) (Raeder et al., 2001), and the Coupled Magnetosphere Ionosphere Thermosphere Model (CMIT) (Wiltberger et al., 2004; W. Wang et al., 2004; Toffoletto et al., 2004). In these approaches, magnetohydrodynamic (MHD) setups coupled with kinetic drift-physics models and ionospheric electrodynamics solvers are used to calculate the Dst, which makes the process computationally very expensive. Given that the draping interplanetary medium changes the structure of a propagating CME in the heliosphere (Pal et al., 2020) and also observed data inputs are possible only at L1 point near Earth there is very little time available to make such forecasts. In this study, we demonstrate the possibility of utilising a physically intuitive MHD modelling of the CME flux rope - magnetosphere interaction to arrive at a reasonable estimate of geoeffectiveness and temporal variations of geomagnetic storms.

We develop a 3D MHD STORM Interaction Module (CESSI-STORMI), in which we focus on a "far-out" planet and the associated magnetosphere. Based on in situ observations at L1 point, we model incoming transients, like solar wind and the ICME, and introduce those into the domain at the day side boundary. In this study, we explore the ICME-magnetosphere interaction and simulate the geoeffectiveness of two different storms from the relatively active Solar Cycle 23 (Gopalswamy, 2006a). The first event (henceforth event 1) occurred on 20 November 2003 which was the strongest geoeffective storm in last three decades (Dst $= -422\,\mathrm{nT}$) with a highly inclined flux rope with a negative z component of the magnetic field (Bz) in the core (Gopalswamy et al., 2005; Cid et al., 2014). The second event (henceforth event 2), occurred on 13 April 2006 and was a stark contrast to the previous one; the flux rope of the associated ICME was low in inclination and had a moderate impact on the Earth's magnetosphere (Dst $= -98\,\mathrm{nT}$). In the subsequent sections we describe the STORMI module, our results, discussions and the conclusions of this study.

2 The STORM Interaction Model Setup

We have developed STORMI based on CESSI-SPIM (Das et al., 2019; Basak & Nandy, 2021) using the magnetohydrodynamic architecture of the open source MHD code, PLUTO (Mignone et al., 2007) (see Text S1). The initialisation of STORMI begins with forcing the planetary dipolar magnetic field with the modelled solar wind and interplanetary magnetic fields (IMFs). The IMF winds from upto 120 minutes before the arrival of the ICME shock are used to establish the magnetospheric steady state as defined by Das et al. (2019). We set the magnetic field components of the IMFs by time averaging the in situ observations from that period gleaned at Lagrange point L1.

In our simulations, the planetary parameters for Earth are same as in Das et al. (2019) except for the density of the ambient medium, which is remodelled to 5.02×10^{-24} gm/cc. The coordinate system is identical to the Geocentric Solar Ecliptic System (GSE), but with a rotation of 180° about the common z-axis. Although Earth's magnetic axis is tilted by an angle of about 11° from the rotation axis; since, for this study, the computational timescale is longer than a day and the modelled Earth is stationary, we consider the rotation axis to be the best possible time-averaged magnetic axis such that the geographic and magnetic equators become coplanar.

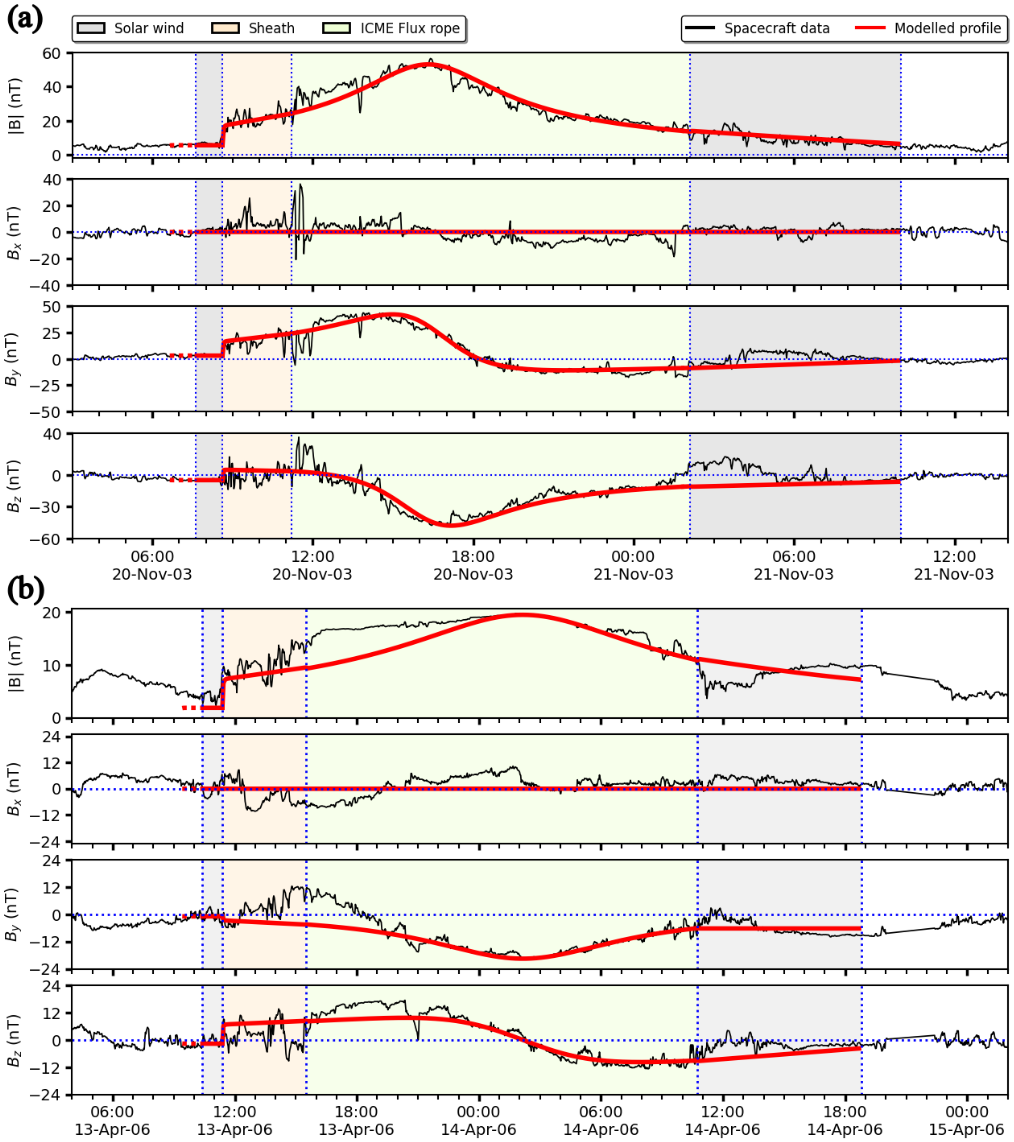

Figure 1. Comparison between the ICME structure embedded in the solar wind (black lines) and the modelled input (red lines) in the GSE coordinate system for event 1 in **(a)** and event 2 in **(b)**, respectively. The initial dotted red line in the modelled profiles corresponds to the solar wind input that forced the magnetosphere to a steady state. The interplanetary conditions are plotted using the Wind Magnetic Field Investigation (MFI) data provided by the NASA Coordinated Data Analysis Web (CDAWeb) service. The modelled profile is measured at a single point on the x-line at the day side domain boundary and then time-shifted to the average x-position of the Wind spacecraft, which was at the night side of Earth ($\sim -213\,\mathrm{R_E}$) for event 1 and at day side ($\sim 199\,\mathrm{R_E}$) for event 2.

In accordance with in situ observations, after the IMF wind, the modelled ICME's shock and sheath region approach Earth, followed by the modelled flux rope (Kilpua et al., 2017). With the realisation that a global structure cannot be exactly matched with single-point measurement, we follow simpler, realistic assumptions to model the ICME. Figures 1 (a) and (b) show the temporal evolution of the observed magnetic field components of the ambient space environment (black curves) and the modelled wind (red curves) for both events, respectively. The magnetic properties of the sheath regions have been adapted to maintain a smooth transition of the structure from sheath to cloud along the x-axis. The low plasma temperature and low plasma β regions in the in situ data help identify the temporal boundaries of the flux ropes (Burlaga et al., 1981). The density and pressure of the ICMEs are defined by solving the Rankine–Hugoniot conditions to generate and maintain the shock fronts. We model the flux ropes using the force-free nonlinear flux rope model developed by Gold and Hoyle (Gold & Hoyle, 1960; Hu et al., 2014; Y. Wang et al., 2016) (see Text S2) which move along the Sun-Earth line (along the x-axis) near 1 AU. Moreover, within the length scale of the domain, which is small compared to the global structure of ICMEs, the central axes of the modelled flux ropes are assumed to be normal to the x-line, and as a result, we get a zero B_x (radial) component inside flux ropes (figure 1). The B_x component is taken to be zero for the sheath and solar wind to ease the divergence cleaning process of the code. Taking into account the negligible expansion rate of the cloud, the time-averaged in situ velocities are used as the velocity of the modelled ICMEs. Following the ICME transit, we again introduce the IMF forcing on the magnetosphere based on time-averaged data for at least another eight hours to simulate the relaxation of the magnetospheric system in the aftermath of the storm.

3 Results

3.1 Magnetospheric dynamics

In both events, before the ICME enters the picture, the initial solar wind forcing leads to a droplet-shaped, steady, dynamic atmosphere of the planetary magnetosphere (Schwartz, 1985; W. Liu & Fujimoto, 2011; Das et al., 2019). The magnetopause forms on the day side, whereas on the night side, the magnetotail shows the cross-sectional θ shaped current systems similar to the plasma regimes observed by Geotail (Christon et al., 1998) in both cases. However, due to the nonzero y-component of the incoming mag-

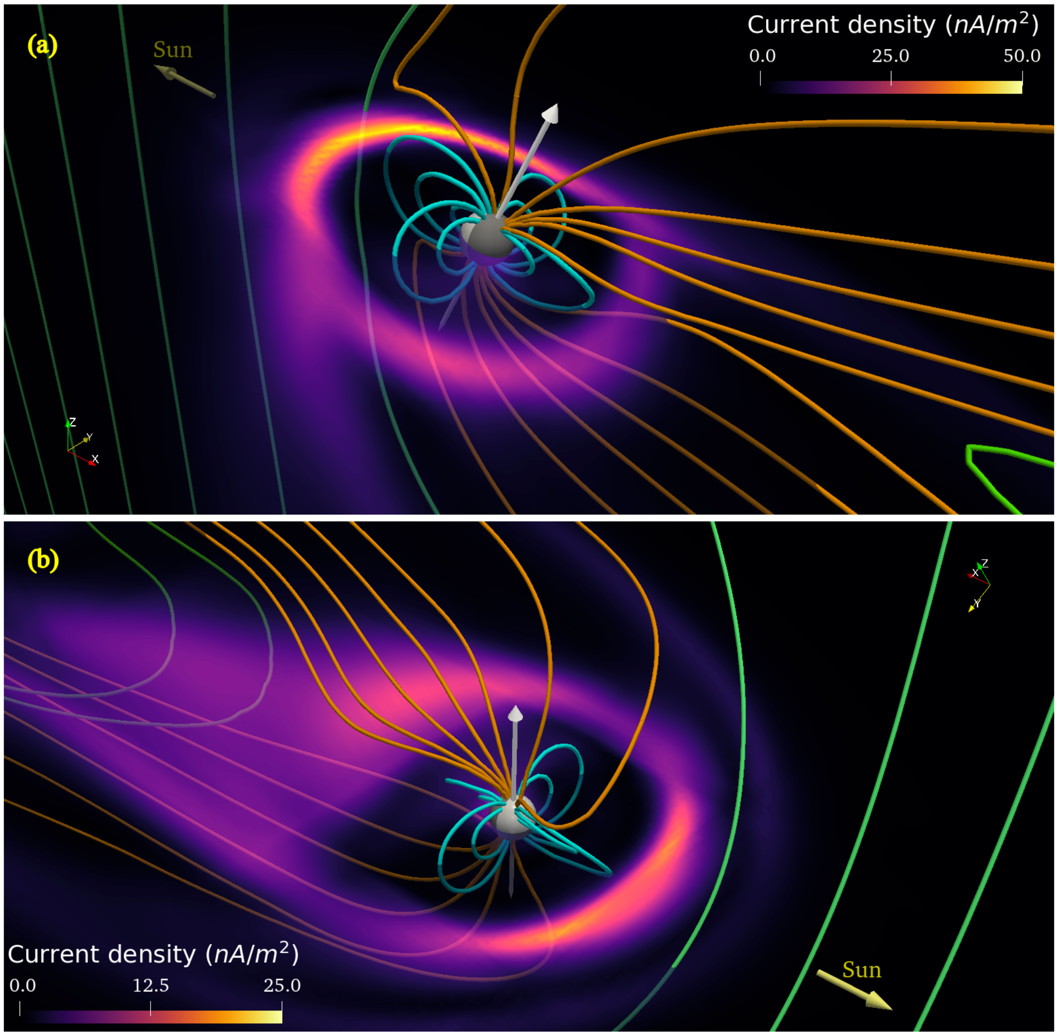

Figure 2. Simulated three-dimensional view of the planetary magnetosphere from a viewpoint just above the ecliptic plane. The magnetosphere is depicted using coloured lines to distinguish between the Earth's polar open magnetic field lines (orange) and closed magnetic field lines (cyan), and IMF (green). The strong event that occurred on 20 November 2003 is shown in panel **(a)** and the moderate event of 14 April 2006 is shown in panel **(b)**. The white arrows in both images denote the rotation axis of Earth. The magnitude of the current density (J) is plotted on the equatorial planes to demonstrate the current formation around the Earth right after the passage of the leading halves of the flux ropes at 17:33 UTC for event 1 and 05:24 UTC for event 2. The yellow arrows designate the Sun-side (along the x-axis).

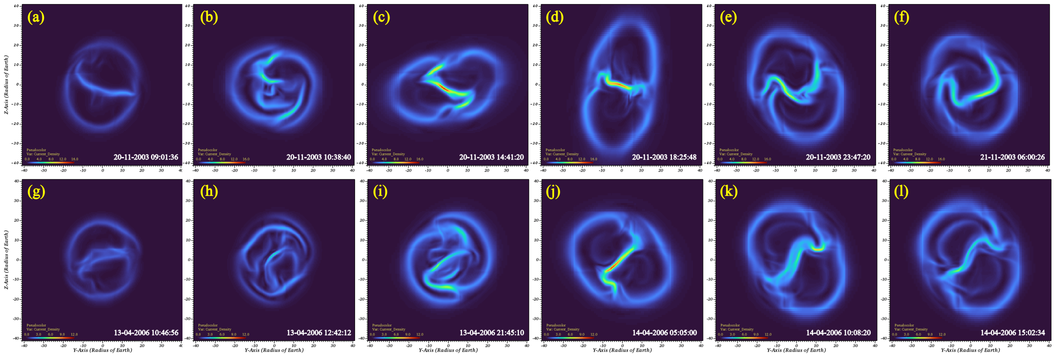

Figure 3. Cross-sectional θ-shaped current systems of the magnetotail for event 1 (top row) and event 2 (bottom row). The current density (J) is plotted in the YZ plane (STORMI's coordinate system) at a distance of $60R_E$ from Earth and is viewed from the magnetotail side. Panels **(a)** and **(g)** in the first and leftmost column show the current boundaries of the magnetotail due to solar wind forcing before the ICME's arrival. In the second column, **(b)** and **(h)** reveal the magnetotail currents during the ICME sheath for the events 1 and 2 respectively. Panel **(c)** and **(i)** show the current system during initial ICME forcing for the events. For the rest of event 1, the magnetotail gets stretched maximally along the semi-major axis as depicted in **(d)** and starts decreasing in **(e)** as the trailing part of the ICME crosses the Earth. In **(f)** the solar wind forcing reshapes the magnetotail away from the perturbed state. On the other hand, **(j)** and **(k)** show the simulated magnetotail during the maximum impact during the transit of the trailing part of the ICME for event 2. Panel **(l)** shows the post-ICME solar wind forced magnetotail.

netic field (B_y), the θ boundary assumes an elliptical shape (see Nakamura et al. (1997)). Magnetic flux conservation between the polar cap and the elliptic magnetotail calculated based on the method described by Kallenrode (2001) puts the boundaries of the polar cap (Sergeev, 1990) around 70.5° latitude for event 1 and around 73° latitude for event 2.

After the initial wind, as soon as the ICME shock arrives at Earth, the magnetosphere experiences extreme compression because of the enormous increase in the ram pressure of the inflow. The day-side magnetopause moves toward Earth by a maximum of $2.5R_E$ for both events. Soon after, it relaxes to a new equilibrium magnetopause standoff distance (R_{mp}) of $9.25R_E$ and $9.75R_E$, respectively. The global magnetosphere undergoes significant perturbations due to the flux ropes passing around the Earth. The planetary magnetic fields start to change their orientation, influenced by the ram pressure and the magnetic topology of the incoming cloud. Figure 2 (a) and (b) shows the 3-dimensional orientation of the magnetosphere and current density at the equatorial planes at 17:33 UTC on 20 November 2003 and at 05:24 UTC on 14 April 2006, respectively, after the leading halves of the modelled flux ropes pass the Earth. The boundary of the simulated polar cap is located around 50° latitude for event 1 during the maximum impact; in situ measurements confirm that it had moved to about 60° of geomagnetic latitude (MLAT) in reality (Ebihara et al., 2005). On the other hand, for event 2, the boundary of the polar cap shifts to around 55° of latitude during the impact of the trailing part of the ICME.

Studies have shown that the magnetotail retains memory of the orientation of the previous IMF states since the impact of the solar wind is first observed at the nose of the magnetosphere, followed by dynamic activities of near-Earth magnetic field lines on the night side and then on the distant magnetotail (Walker et al., 1999; Hultqvist et al., 1999). We observe that the time-varying structure of the magnetic clouds introduces torsion into the magnetotail. Figure 3 depicts the simulated time-varying magnetosphere in terms of the cross-sectional current of the magnetotail for the events. During quiet time, the three-dimensional orientation of the geomagnetic dipole decides the orientation of the semi-major axis of the elliptical current system in the magnetotail. However, during the storm, the magnetic forces (and reconnections) acting on the field lines at the polar-cap boundary make the magnetotail cross-section more tilted and elongated because of the flux rope. We notice that the stretching enhances along the semi-major axis with time and becomes maximum when the incoming magnetic field becomes anti-parallel to the dipole axis. Nevertheless, after the passing of the cloud, the modelled solar wind compensates for the stretch with time due to the orientation of the field lines.

3.2 A New Method for Estimating Geomagnetic Storm Intensity Using the Simulated STORMI Index

During a storm, disturbances in the magnetosphere are measured by Dst and SYM-H indices, which are known to be primarily produced by magnetospheric ring currents. These currents are generated by the perturbed ionosphere and trapped solar wind particles that undergo gyromotion, grad-B drift motion, and curvature drift motion within the magnetosphere (Parker, 1957; Williams, 1983; Roelof & Williams, 1988; Daglis et al., 1999; Daglis, 2001; Le et al., 2004; Ganushkina et al., 2017; Ebihara, 2019). Thus, during geomagnetic storms, the enhancement in the entrapped charged particles and the dawn-dusk asymmetry of the magnetic fields increase these currents. This happens in such a way that the geomagnetic field becomes weak, implying a reduction in the Dst and SYM-H values.

In our model, we observe currents in the form $\vec{J} = c\,(\vec{\nabla} \times \vec{B})$ (see Text S1), induced by the magnetic field topology around Earth and influenced by plasma flows. Images 2 (a) and (b) show the distribution of the current density (J) in the equatorial plane of the magnetosphere after the passage of the leading halves of the flux ropes for both events. Within the magnetosphere these induced currents exhibit a behaviour similar to that of the equatorial ring currents (Le et al., 2004) and are directed eastward within $\sim 3R_E$, and westward within $\sim 4{-}7R_E$ (Roy & Nandy, 2021a, 2021b). The modelled magnetopause boundary current also flows from the west to the east, as seen in Stern (1994). We observe a significant increase in the magnitude of these currents while the ICME crosses the Earth. Based on these observations, we calculate the STORM Intensity (STORMI) index (as a modelled proxy for the Dst and SYM-H indices) to estimate the geoeffectiveness using these induced magnetospheric currents. To achieve this we use the integral form of the Biot-Savart's law (with usual notations),

$$\vec{B}(r) = \frac{1}{c}\int_{v'} \frac{\vec{J}(r') \times \vec{r}'}{r'^3} dv'.$$

We assume a geocentric conductor focusing on the equatorial plane and covering the magnetosphere and the plasma atmosphere of the modelled planet with an inner radius of 1.5 R_E (leaving two grid cells from the planetary surface) and an outer radius of 6.5 R_E. At twelve equatorial grid points (see Figure S1) and two polar grid points just outside the planet, we calculate the axial component (parallel to the dipole axis) of the magnetic field for the current distribution throughout the volume (v') of the plasma sphere. The thickness of the conductor is fixed for each event based on the initial distribution of the current near the equatorial plane. For event 1 it is 1.9 R_E, whereas it is 1.6 R_E for event 2. We plot the equatorial current distribution by plotting the time-averaged quiet-time current density, surface-averaged over circular planes parallel to the equator to estimate the width of the distribution near the equator as a function of their distance (see figure S2). We take the mean contribution from all fourteen points to calculate the global induced field. The field due to the initial solar wind is designated as the quiet-time baseline and it is set to be equal to the corresponding SYM-H value. We estimate the STORMI index by calculating the change in induced magnetic field during the ICME passage with respect to the baseline.

In the figures of 4 (a) and (b), the blue curve shows the progression of the STORMI index with time for both events, along with the shaded blue regions showing the span of the standard deviation (σ) at each time. For event 1, the modelled ICME's shock gives a sudden increase in STORMI index value reminiscent of storm sudden commencement. However, as the shock propagates, the suppressed magnetic fields lead to a negative jump in the STORMI index with a large induced current for a short time. Once the sheath region starts after the ICME shock, the STORMI index starts decreasing with an increasing negative B_z and stronger induced current in the equatorial regions. On the contrary, after the sudden commencement and passage of the shock, the STORMI index remains positive with respect to the baseline for event 2. This is mainly due to induced eastward currents because of the positive B_z of the incoming flow. As the flux rope enters the domain, the reduction in the field enhances for event 1, making the index more negative with time. It increases rapidly, reaching a maximum value (with σ bound) of $-523.9\pm 98\,\mathrm{nT}$ at 17:03 UTC on 20 November 2003, just a few minutes after the flux rope's negative B_z core reaches the Earth. After that, the depression of the field starts to recover, and as the solar wind in the aftermath of the ICME takes over, the storm index slowly relaxes. For event 2, the index remains steady for a while and then falls slowly with time as the leading part of the ICME exhibits a positive B_z. However, as soon as B_z changes polarity for event 2, we see a rapid fall in the index, which goes to a moderately low value of $-114.6 \pm 34\,\mathrm{nT}$ at 11:19 UTC on 14 April 2006. In this case too, we see a slow recovery of the index as the solar wind replaces the ICME and the system relaxes.

The minimum Dst value for event 1 was $-422\,\mathrm{nT}$, recorded at 20:00 UTC, whereas the minimum SYM-H was $-490\,\mathrm{nT}$, recorded at 18:17 UTC. The Dst and SYM-H values for event 2 were $-98\,\mathrm{nT}$ and $-111\,\mathrm{nT}$ recorded at 09:00 UTC and 09:21 UTC on 14 April 2006, respectively. For qualitative comparisons, we plot the real-time values of Dst and SYM-H in black dashed and solid curves in figure 4. For the quantitative analysis of temporal variations, we mainly follow the guidelines prescribed by M. W. Liemohn et al. (2018). For both events, the observed and modelled indices exhibit a linear relationship between the STORMI index and Dst and SYM-H. The Pearson correlation coefficients are more than 0.83 and 0.88 (with 99.99% confidence) for Dst and SYM-H prediction respectively for event 1. The same are 0.95 and 0.93 (with 99.99% confidence)

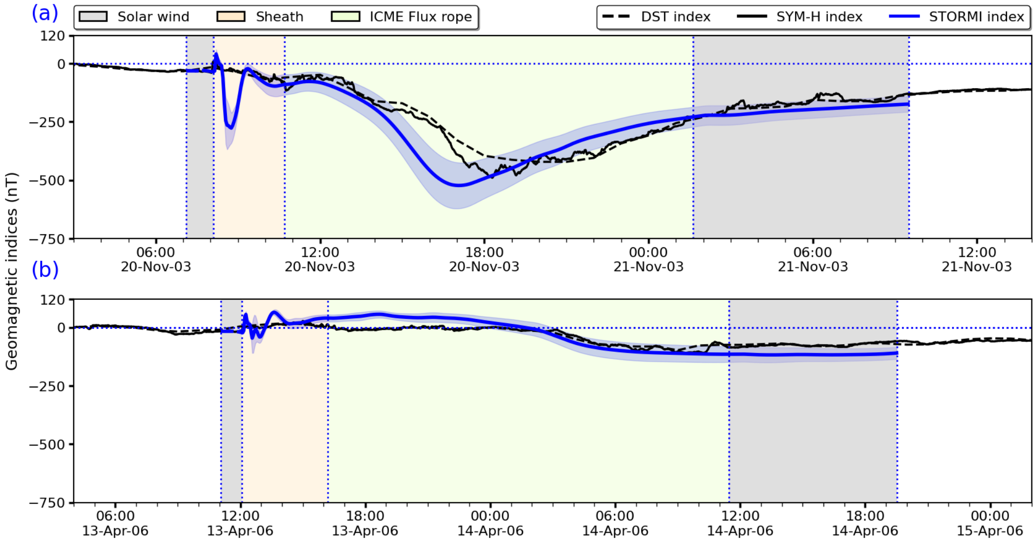

Figure 4. The figure presents the comparison of the time evolution of the Dst index (black dashed curve), SYM-H index (black solid line), and the modelled reduction in the geomagnetic field intensity in terms of STORMI index (blue curve) for event 1 in panel **(a)** and for event 2 in panel **(b)**. The transparent blue shaded region is the standard deviation of the STORMI geomagnetic storm index. The STORMI index is computed after incorporating the time delay between the in situ observations of solar wind (shown in figure 1) and geomagnetic perturbation. A quantitative analysis of the results is given in Table S1

respectively for event 2. The normalised root mean squared (NRMS) error in our values lie within $0.12 \sim 0.19$, as normalised over the range of modelled values. We get a positive prediction efficiency (PE) for all the cases with a maximum of 0.71 which implies that the modelled values are better at reproducing the observed values than any random sample of the observation (Murphy, 1988). Table S1 summarises the efficiency of STORMI in predicting these events based on linearity, Pearson correlation coefficient, normalised RMS error and prediction efficiency.

4 Discussion and Conclusions

We develop a 3D MHD module called CESSI-STORMI to simulate the interaction of ICMEs with planetary magnetospheres. Instead of mapping a single point observation to a 2D (in-flowing) boundary, we use Gold-Hoyle type magnetic flux ropes to model the ICMEs for a more physical representation of the global magnetic structure of the storm. We introduce the simulated STORMI index to quantify the geo-effectiveness of the events. This index estimates the reduced magnetic field – averaged over fourteen different points around the modelled Earth — due to induced currents in the equatorial region of the simulated magnetosphere. We utilise Biot-Savart's law for this estimation.

Some discrepancy between our simulations and observations are expected as we use single-fluid MHD modelling approximation and do not consider magnetospheric current systems like magnetopause and cross-tail currents (Maltsev, 2004). By sacrificing intricate complexities, we focus on the development of a simple, time-efficient modelling framework with reasonably good prediction skills.

We simulate two contrasting (strong and moderate) geomagnetic storm events and demonstrate a very good correlation between observed and simulated geoeffectiveness and the time of occurrence for the maximum impact. A quantitative analysis recovers a strong linear correlation between the predicted STORMI index and observed Dst and SYM-H, thus validating our approach and the utility of the STORMI index.

Additionally, we also calculate the shift in the latitude of the polar-cap boundary by adapting a flux-conservation equation for an ellipse. We investigate the reshaping of the magnetosphere with time due to the ICME's helical magnetic fields and observe the impact of the imposed torsion in the magnetotail (see Movies S1-S4) which illuminates the global dynamics at play.

Prior forecasting of the magnetic structure and orientation of a CME (and its counterpart ICME) remains challenging (Kilpua et al., 2019). However, with advances in machine-learning based prediction of solar flares (Sinha et al., 2022) and prediction of properties of ICME magnetic clouds based on near sun observations (Pal et al., 2018; Pal, Sanchita et al., 2022) early knowledge of the possibility and properties of solar magnetic storms may be possible. We emphasise that with knowledge of the magnetic and kinematic properties of CMEs a few days in advance, CESSI-STORMI can be utilised at an even earlier phase for predicting the timing and intensity of geomagnetic storms.

5 Open Research

The simulation data underlying this article will be shared on reasonable request to the corresponding author. The in situ solar wind data from the Wind spacecraft's Magnetic Field Instrument (MFI) (Lepping et al., 1995) and Solar Wind Experiment (SWE) (Ogilvie et al., 1995) has been obtained from the NASA Coordinated Data Analysis Web (CDAWeb) service (*url: https://cdaweb.gsfc.nasa.gov*). The Dst and SYM-H data has been acquired from the Geomagnetic Data Service by World Data Center for Geomagnetism, Kyoto (*url: https://wdc.kugi.kyoto-u.ac.jp/wdc/Sec3.html*). The simulations are performed using open source code PLUTO (Mignone et al., 2007) (*url: http://plutocode.ph.unito.it/*). The data visualisations are done using the following open source tools: VisIt (version 3.1.2) (Childs et al., 2012) (*url: https://visit-dav.github.io/visit-website/*), ParaView (version 5.8.1) (Ahrens et al., 2005; Ayachit, 2015) (*url: https://www.paraview.org/*), pyPLUTO (*url: https://gitlab.mpcdf.mpg.de/sdoetsch/pypluto*), Matplotlib (version 3.4.2) (*url: https://matplotlib.org/*) and Pillow (version 9.2.0) (*url: https://pillow.readthedocs.io/en/stable/*).

Acknowledgments

The Center of Excellence in Space Sciences India (CESSI) is funded by the Ministry of Education, Government of India. Souvik Roy acknowledges the financial support from the Human Resource Development Group (HRDG) of the Council of Scientific and Industrial Research (CSIR), India. The authors thank Bhargav Vaidya, Srijan B. Das, Sanchita Pal, Arnab Basak, Sanghita Chandra, Yoshita Baruah, Priyansh Jaswal for their thoughtful insights and comments. We are also grateful to Prosenjit Lahiri for his contributions to maintaining the computational infrastructure at CESSI.

References

Ahrens, J., Geveci, B., & Law, C. (2005). 36 - paraview: An end-user tool for large-data visualization. In C. D. Hansen & C. R. Johnson (Eds.), *Visualization handbook* (p. 717-731). Burlington: Butterworth-Heinemann. Retrieved from `https://www.sciencedirect.com/science/article/pii/B9780123875822500381` doi: https://doi.org/10.1016/B978-012387582-2/50038-1

Ayachit, U. (2015). *The paraview guide: A parallel visualization application.* Clifton Park, NY, USA: Kitware, Inc.

Basak, A., & Nandy, D. (2021, 01). Modelling the imposed magnetospheres of Mars-like exoplanets: star–planet interactions and atmospheric losses. *Monthly Notices of the Royal Astronomical Society*, *502*(3), 3569-3581. Retrieved from `https://doi.org/10.1093/mnras/stab225` doi: 10.1093/mnras/stab225

Bhowmik, P., & Nandy, D. (2018, Dec 06). Prediction of the strength and timing of sunspot cycle 25 reveal decadal-scale space environmental conditions. *Nature Communications*, *9*(1), 5209. Retrieved from `https://doi.org/10.1038/s41467-018-07690-0` doi: 10.1038/s41467-018-07690-0

Burlaga, L. F., Klein, L., Sheeley Jr., N. R., Michels, D. J., Howard, R. A., Koomen, M. J., … Rosenbauer, H. (1982). A magnetic cloud and a coronal mass ejection. *Geophysical Research Letters*, *9*(12), 1317-1320. Retrieved from `https://agupubs.onlinelibrary.wiley.com/doi/abs/10.1029/GL009i012p01317` doi: https://doi.org/10.1029/GL009i012p01317

Burlaga, L. F., Sittler, E., Mariani, F., & Schwenn, R. (1981). Magnetic loop behind an interplanetary shock: Voyager, helios, and imp 8 observations. *Journal of Geophysical Research: Space Physics*, *86*(A8), 6673-6684. Retrieved from `https://agupubs.onlinelibrary.wiley.com/doi/abs/10.1029/JA086iA08p06673` doi: https://doi.org/10.1029/JA086iA08p06673

Childs, H., Brugger, E., Whitlock, B., Meredith, J., Ahern, S., Pugmire, D., … Navrátil, P. (2012, October). Visit: An end-user tool for visualizing and analyzing very large data. In *High performance visualization–enabling extreme-scale scientific insight* (p. 357-372). doi: 10.1201/b12985

Christon, S. P., Eastman, T. E., Doke, T., Frank, L. A., Gloeckler, G., Kojima, H., … Yamamoto, T. (1998). Magnetospheric plasma regimes identified using geotail measurements: 2. statistics, spatial distribution, and geomagnetic dependence. *Journal of Geophysical Research: Space Physics*, *103*(A10), 23521-23542. Retrieved from `https://agupubs.onlinelibrary.wiley.com/doi/abs/10.1029/98JA01914` doi: https://doi.org/10.1029/98JA01914

Cid, C., Palacios, J., Saiz, E., Guerrero, A., & Cerrato, Y. (2014). On extreme geomagnetic storms. *J. Space Weather Space Clim.*, *4*, A28. Retrieved from `https://doi.org/10.1051/swsc/2014026` doi: 10.1051/swsc/2014026

Daglis, I. A. (2001, Aug 01). The storm-time ring current. *Space Science Reviews*, *98*(3), 343-363. Retrieved from `https://doi.org/10.1023/A:1013873329054` doi: 10.1023/A:1013873329054

Daglis, I. A., Thorne, R. M., Baumjohann, W., & Orsini, S. (1999). The terrestrial ring current: Origin, formation, and decay. *Reviews of Geophysics*, *37*(4), 407-438. Retrieved from `https://agupubs.onlinelibrary.wiley.com/doi/abs/10.1029/1999RG900009` doi: https://doi.org/10.1029/1999RG900009

Das, S. B., Basak, A., Nandy, D., & Vaidya, B. (2019, may). Modeling star–planet interactions in far-out planetary and exoplanetary systems. *The Astrophysical Journal*, *877*(2), 80. Retrieved from `https://doi.org/10.3847/1538-4357/ab18ad` doi: 10.3847/1538-4357/ab18ad

Ebihara, Y. (2019, Feb 13). Simulation study of near-earth space disturbances: 1. magnetic storms. *Progress in Earth and Planetary Science*, *6*(1), 16. Retrieved from `https://doi.org/10.1186/s40645-019-0264-3` doi: 10.1186/s40645-019-0264-3

Ebihara, Y., Fok, M.-C., Sazykin, S., Thomsen, M. F., Hairston, M. R., Evans, D. S., … Ejiri, M. (2005). Ring current and the magnetosphere-ionosphere coupling during the superstorm of 20 november 2003. *Journal of Geophysical Research: Space Physics*, *110*(A9). Retrieved from `https://agupubs.onlinelibrary.wiley.com/doi/abs/10.1029/2004JA010924` doi: https://doi.org/10.1029/2004JA010924

Ganushkina, N., Jaynes, A., & Liemohn, M. (2017, Nov 01). Space weather effects produced by the ring current particles. *Space Science Reviews*, *212*(3), 1315-1344. Retrieved from `https://doi.org/10.1007/s11214-017-0412-2` doi: 10.1007/s11214-017-0412-2

Gold, T., & Hoyle, F. (1960, 02). On the Origin of Solar Flares. *Monthly Notices of* *the Royal Astronomical Society*, *120*(2), 89-105. Retrieved from `https://doi.org/10.1093/mnras/120.2.89` doi: 10.1093/mnras/120.2.89

Gonzalez, W. D., Joselyn, J. A., Kamide, Y., Kroehl, H. W., Rostoker, G., Tsurutani, B. T., & Vasyliunas, V. M. (1994). What is a geomagnetic storm? *Journal of Geophysical Research: Space Physics*, *99*(A4), 5771-5792. Retrieved from `https://agupubs.onlinelibrary.wiley.com/doi/abs/10.1029/93JA02867` doi: https://doi.org/10.1029/93JA02867

Gopalswamy, N. (2002). Relation between coronal mass ejections and their interplanetary counterparts. In H. Wang & R. Xu (Eds.), *Solar-terrestrial magnetic activity and space environment* (Vol. 14, p. 157-164). Pergamon. Retrieved from `https://www.sciencedirect.com/science/article/pii/S0964274902801482` doi: https://doi.org/10.1016/S0964-2749(02)80148-2

Gopalswamy, N. (2004). A global picture of cmes in the inner heliosphere. In G. Poletto & S. T. Suess (Eds.), *The sun and the heliosphere as an integrated system* (pp. 201–251). Dordrecht: Springer Netherlands. Retrieved from `https://doi.org/10.1007/978-1-4020-2831-1_8` doi: 10.1007/978-1-4020-2831-1_8

Gopalswamy, N. (2006a, Jun 01). Coronal mass ejections of solar cycle 23. *Journal of Astrophysics and Astronomy*, *27*(2), 243-254. Retrieved from `https://doi.org/10.1007/BF02702527` doi: 10.1007/BF02702527

Gopalswamy, N. (2006b, Jun 01). Properties of interplanetary coronal mass ejections. *Space Science Reviews*, *124*(1), 145-168. Retrieved from `https://doi.org/10.1007/s11214-006-9102-1` doi: 10.1007/s11214-006-9102-1

Gopalswamy, N., Mewaldt, R., & Torsti, J. (2006, January). Solar Eruptions and Energetic Particles. *Washington DC American Geophysical Union Geophysical Monograph Series*, *165*. doi: 10.1029/GM165

Gopalswamy, N., Yashiro, S., Michalek, G., Xie, H., Lepping, R. P., & Howard, R. A. (2005). Solar source of the largest geomagnetic storm of cycle 23. *Geophysical Research Letters*, *32*(12). Retrieved from `https://agupubs.onlinelibrary.wiley.com/doi/abs/10.1029/2004GL021639` doi: https://doi.org/10.1029/2004GL021639

Gosling, J. T. (1990). Coronal mass ejections and magnetic flux ropes in interplanetary space. In *Physics of magnetic flux ropes* (p. 343-364). American

Geophysical Union (AGU). Retrieved from `https://agupubs.onlinelibrary.wiley.com/doi/abs/10.1029/GM058p0343` doi: https://doi.org/10.1029/GM058p0343

Hu, Q., Qiu, J., Dasgupta, B., Khare, A., & Webb, G. M. (2014, sep). STRUCTURES OF INTERPLANETARY MAGNETIC FLUX ROPES AND COMPARISON WITH THEIR SOLAR SOURCES. *The Astrophysical Journal*, *793*(1), 53. Retrieved from `https://doi.org/10.1088/0004-637x/793/1/53` doi: 10.1088/0004-637x/793/1/53

Hultqvist, B., Øieroset, M., Paschmann, G., & Treumann, R. A. (1999). Source and loss processes in the magnetotail. In B. Hultqvist, M. Øieroset, G. Paschmann, & R. A. Treumann (Eds.), *Magnetospheric plasma sources and losses: Final report of the issi study project on source and loss processes* (pp. 285–353). Dordrecht: Springer Netherlands. Retrieved from `https://doi.org/10.1007/978-94-011-4477-3_6` doi: 10.1007/978-94-011-4477-3_6

Iyemori, T., Takeda, M., Nose, M., Odagi, Y., & Toh, H. (2009). Mid-latitude geomagnetic indices ”asy” and ”sym” for 2009 (provisional). Data Analysis Center for Geomagnetism and Space Magnetism, Graduate School of Science,Kyoto University, Japan. Retrieved from `http://wdc.kugi.kyoto-u.ac.jp/aeasy/asy.pdf`

Kallenrode, M.-B. (2001). The terrestrial magnetosphere. In *Space physics: An introduction to plasmas and particles in the heliosphere and magnetospheres* (pp. 217–284). Berlin, Heidelberg: Springer Berlin Heidelberg. Retrieved from `https://doi.org/10.1007/978-3-662-04443-8_8` doi: 10.1007/978-3-662-04443-8_8

Kilpua, E., Koskinen, H. E. J., & Pulkkinen, T. I. (2017, Nov 24). Coronal mass ejections and their sheath regions in interplanetary space. *Living Reviews in Solar Physics*, *14*(1), 5. Retrieved from `https://doi.org/10.1007/s41116-017-0009-6` doi: 10.1007/s41116-017-0009-6

Kilpua, E., Lugaz, N., Mays, M. L., & Temmer, M. (2019). Forecasting the structure and orientation of earthbound coronal mass ejections. *Space Weather*, *17*(4), 498-526. Retrieved from `https://agupubs.onlinelibrary.wiley.com/doi/abs/10.1029/2018SW001944` doi: https://doi.org/10.1029/2018SW001944

Lakhina, G. S., & Tsurutani, B. T. (2016, Feb 20). Geomagnetic storms: historical perspective to modern view. *Geoscience Letters*, *3*(1), 5. Retrieved from `https://doi.org/10.1186/s40562-016-0037-4` doi: 10.1186/s40562-016-0037-4

Le, G., Russell, C. T., & Takahashi, K. (2004). Morphology of the ring current derived from magnetic field observations. *Annales Geophysicae*, *22*(4), 1267–1295. Retrieved from `https://angeo.copernicus.org/articles/22/1267/2004/` doi: 10.5194/angeo-22-1267-2004

Lepping, R. P., Acũna, M. H., Burlaga, L. F., Farrell, W. M., Slavin, J. A., Schatten, K. H., … Worley, E. M. (1995, Feb 01). The wind magnetic field investigation. *Space Science Reviews*, *71*(1), 207-229. Retrieved from `https://doi.org/10.1007/BF00751330` doi: 10.1007/BF00751330

Liemohn, M., Ganushkina, N. Y., De Zeeuw, D. L., Rastaetter, L., Kuznetsova, M., Welling, D. T., … van der Holst, B. (2018). Real-time swmf at ccmc: Assessing the dst output from continuous operational simulations. *Space Weather*, *16*(10), 1583-1603. Retrieved from `https://agupubs.onlinelibrary.wiley.com/doi/abs/10.1029/2018SW001953` doi: https://doi.org/10.1029/2018SW001953

Liemohn, M. W., McCollough, J. P., Jordanova, V. K., Ngwira, C. M., Morley, S. K., Cid, C., … Vasile, R. (2018). Model evaluation guidelines for geomagnetic index predictions. *Space Weather*, *16*(12), 2079-2102. Retrieved from `https://agupubs.onlinelibrary.wiley.com/doi/abs/10.1029/2018SW002067` doi: https://doi.org/10.1029/2018SW002067

Liu, W., & Fujimoto, M. (Eds.). (2011). *The dynamic magnetosphere* (1st ed.). Springer, Dordrecht. Retrieved from `https://doi.org/10.1007/978-94-007-0501-2` doi: 10.1007/978-94-007-0501-2

Liu, Y. D., Luhmann, J. G., Kajdič, P., Kilpua, E. K., Lugaz, N., Nitta, N. V., … Galvin, A. B. (2014, Mar 18). Observations of an extreme storm in interplanetary space caused by successive coronal mass ejections. *Nature Communications*, *5*(1), 3481. Retrieved from `https://doi.org/10.1038/ncomms4481` doi: 10.1038/ncomms4481

Love, J. J. (2021). Extreme-event magnetic storm probabilities derived from rank statistics of historical dst intensities for solar cycles 14–24. *Space Weather*, *19*(4), e2020SW002579. Retrieved from `https://agupubs.onlinelibrary`

`.wiley.com/doi/abs/10.1029/2020SW002579` (e2020SW002579 2020SW002579) doi: https://doi.org/10.1029/2020SW002579

Maltsev, Y. P. (2004, Jan 01). Points of controversy in the study of magnetic storms. *Space Science Reviews*, *110*(3), 227-267. Retrieved from `https://doi.org/10.1023/B:SPAC.0000023410.77752.30` doi: 10.1023/B:SPAC.0000023410.77752.30

Menvielle, M., Iyemori, T., Marchaudon, A., & Nosé, M. (2011). Geomagnetic indices. In M. Mandea & M. Korte (Eds.), *Geomagnetic observations and models* (pp. 183–228). Dordrecht: Springer Netherlands. Retrieved from `https://doi.org/10.1007/978-90-481-9858-0_8` doi: 10.1007/978-90-481-9858-0_8

Mignone, A., Bodo, G., Massaglia, S., Matsakos, T., Tesileanu, O., Zanni, C., & Ferrari, A. (2007, may). PLUTO: A numerical code for computational astrophysics. *The Astrophysical Journal Supplement Series*, *170*(1), 228–242. Retrieved from `https://doi.org/10.1086/513316` doi: 10.1086/513316

Murphy, A. H. (1988). Skill scores based on the mean square error and their relationships to the correlation coefficient. *Monthly Weather Review*, *116*(12), 2417 - 2424. Retrieved from `https://journals.ametsoc.org/view/journals/mwre/116/12/1520-0493_1988_116_2417_ssbotm_2_0_co_2.xml` doi: 10.1175/1520-0493(1988)116⟨2417:SSBOTM⟩2.0.CO;2

Nakamura, R., Kokubun, S., Mukai, T., & Yamamoto, T. (1997). Changes in the distant tail configuration during geomagnetic storms. *Journal of Geophysical Research: Space Physics*, *102*(A5), 9587-9601. Retrieved from `https://agupubs.onlinelibrary.wiley.com/doi/abs/10.1029/97JA00095` doi: https://doi.org/10.1029/97JA00095

Nandy, D. (2021, Mar 24). Progress in solar cycle predictions: Sunspot cycles 24–25 in perspective. *Solar Physics*, *296*(3), 54. Retrieved from `https://doi.org/10.1007/s11207-021-01797-2` doi: 10.1007/s11207-021-01797-2

Nandy, D., Martens, P. C. H., Obridko, V., Dash, S., & Georgieva, K. (2021, Jul 05). Solar evolution and extrema: current state of understanding of long-term solar variability and its planetary impacts. *Progress in Earth and Planetary Science*, *8*(1), 40. Retrieved from `https://doi.org/10.1186/s40645-021-00430-x` doi: 10.1186/s40645-021-00430-x

Ngwira, C. M., Pulkkinen, A., Kuznetsova, M. M., & Glocer, A. (2014). Modeling extreme "carrington-type" space weather events using three-dimensional global mhd simulations. *Journal of Geophysical Research: Space Physics*, *119*(6), 4456-4474. Retrieved from `https://agupubs.onlinelibrary.wiley.com/doi/abs/10.1002/2013JA019661` doi: https://doi.org/10.1002/2013JA019661

Ogilvie, K. W., Chornay, D. J., Fritzenreiter, R. J., Hunsaker, F., Keller, J., Lobell, J., … Gergin, E. (1995, Feb 01). Swe, a comprehensive plasma instrument for the wind spacecraft. *Space Science Reviews*, *71*(1), 55-77. Retrieved from `https://doi.org/10.1007/BF00751326` doi: 10.1007/BF00751326

Pal, S., Dash, S., & Nandy, D. (2020). Flux erosion of magnetic clouds by reconnection with the sun's open flux. *Geophysical Research Letters*, *47*(8), e2019GL086372. Retrieved from `https://agupubs.onlinelibrary.wiley.com/doi/abs/10.1029/2019GL086372` (e2019GL086372 10.1029/2019GL086372) doi: https://doi.org/10.1029/2019GL086372

Pal, S., Nandy, D., Srivastava, N., Gopalswamy, N., & Panda, S. (2018, sep). Dependence of coronal mass ejection properties on their solar source active region characteristics and associated flare reconnection flux. *The Astrophysical Journal*, *865*(1), 4. Retrieved from `https://doi.org/10.3847/1538-4357/aada10` doi: 10.3847/1538-4357/aada10

Pal, Sanchita, Nandy, Dibyendu, & Kilpua, Emilia K. J. (2022). Magnetic cloud prediction model for forecasting space weather relevant properties of earth-directed coronal mass ejections. *A&A*, *665*, A110. Retrieved from `https://doi.org/10.1051/0004-6361/202243513` doi: 10.1051/0004-6361/202243513

Parker, E. N. (1957, Aug). Newtonian development of the dynamical properties of ionized gases of low density. *Phys. Rev.*, *107*, 924–933. Retrieved from `https://link.aps.org/doi/10.1103/PhysRev.107.924` doi: 10.1103/PhysRev.107.924

Raeder, J., Wang, Y., & Fuller-Rowell, T. J. (2001). Geomagnetic storm simulation with a coupled magnetosphere-ionosphere-thermosphere model. In *Space weather* (p. 377-384). American Geophysical Union (AGU). Retrieved from `https://agupubs.onlinelibrary.wiley.com/doi/abs/10.1029/GM125p0377` doi: https://doi.org/10.1029/GM125p0377

Rastätter, L., Kuznetsova, M. M., Glocer, A., Welling, D., Meng, X., Raeder, J., ... Gannon, J. (2013). Geospace environment modeling 2008–2009 challenge: Dst index. *Space Weather*, *11*(4), 187-205. Retrieved from `https://agupubs.onlinelibrary.wiley.com/doi/abs/10.1002/swe.20036` doi: https://doi.org/10.1002/swe.20036

Roelof, E. C., & Williams, D. J. (1988, 6). Terrestrial ring current - from in situ measurements to global images using energetic neutral atoms. *Johns Hopkins APL Tech. Dig.; (United States)*, *9*. Retrieved from `https://www.osti.gov/biblio/6555356`

Roy, S., & Nandy, D. (2021a). Magnetohydrodynamical understanding of the interactions between coronal mass ejections and earth's magnetosphere. *Earth and Space Science Open Archive*, 18. Retrieved from `https://doi.org/10.1002/essoar.10505902.1` doi: 10.1002/essoar.10505902.1

Roy, S., & Nandy, D. (2021b, April). Modelling the Impact of Magnetic Storms on Planetary Environments. In *Egu general assembly conference abstracts* (p. EGU21-8863). Retrieved from `https://doi.org/10.5194/egusphere-egu21-8863` doi: 10.5194/egusphere-egu21-8863

Schrijver, C. J. (2015). Socio-economic hazards and impacts of space weather: The important range between mild and extreme. *Space Weather*, *13*(9), 524-528. Retrieved from `https://agupubs.onlinelibrary.wiley.com/doi/abs/10.1002/2015SW001252` doi: https://doi.org/10.1002/2015SW001252

Schrijver, C. J., Kauristie, K., Aylward, A. D., Denardini, C. M., Gibson, S. E., Glover, A., ... Vilmer, N. (2015). Understanding space weather to shield society: A global road map for 2015–2025 commissioned by cospar and ilws. *Advances in Space Research*, *55*(12), 2745-2807. Retrieved from `https://www.sciencedirect.com/science/article/pii/S0273117715002252` doi: https://doi.org/10.1016/j.asr.2015.03.023

Schwartz, S. J. (1985). Solar wind and the earth's bow shock. In E. R. Priest (Ed.), *Solar system magnetic fields* (pp. 190–223). Dordrecht: Springer Netherlands. Retrieved from `https://doi.org/10.1007/978-94-009-5482-3_8` doi: 10.1007/978-94-009-5482-3_8

Sergeev, V. A. (1990). Polar cap and cusp boundaries at day and night. *Journal of geomagnetism and geoelectricity*, *42*(6), 683-695. doi: 10.5636/jgg.42.683

Sinha, S., Gupta, O., Singh, V., Lekshmi, B., Nandy, D., Mitra, D., … Pal, S. (2022, aug). A comparative analysis of machine-learning models for solar flare forecasting: Identifying high-performing active region flare indicators. *The Astrophysical Journal*, *935*(1), 45. Retrieved from `https://doi.org/10.3847/1538-4357/ac7955` doi: 10.3847/1538-4357/ac7955

Sinha, S., Srivastava, N., & Nandy, D. (2019, jul). Solar filament eruptions as precursors to flare–CME events: Establishing the temporal connection. *The Astrophysical Journal*, *880*(2), 84. Retrieved from `https://doi.org/10.3847/1538-4357/ab2239` doi: 10.3847/1538-4357/ab2239

Stern, D. P. (1994). The art of mapping the magnetosphere. *Journal of Geophysical Research: Space Physics*, *99*(A9), 17169-17198. Retrieved from `https://agupubs.onlinelibrary.wiley.com/doi/abs/10.1029/94JA01239` doi: https://doi.org/10.1029/94JA01239

Sugiura, M., & Kamei, T. (1991). Equatorial dst index 1957-1986. In A. Berthelier & M. Menvielle (Eds.), *International union of geodesy and geophysics association of geomagnetism and aeronomy (iaga) bulletin number 40.* ISGI PUBLICATIONS OFFICE, FRANCE. Retrieved from `http://isgi.unistra.fr/IAGABulletins/IAGA_Bulletin_40_Sugiura_Kamei_1991.pdf` (`http://wdc.kugi.kyoto-u.ac.jp/dstdir/dst2/onDstindex.html`)

Toffoletto, F., Sazykin, S., Spiro, R., Wolf, R., & Lyon, J. (2004). Rcm meets lfm: initial results of one-way coupling. *Journal of Atmospheric and Solar-Terrestrial Physics*, *66*(15), 1361-1370. Retrieved from `https://www.sciencedirect.com/science/article/pii/S1364682604001452` (Towards an Integrated Model of the Space Weather System) doi: https://doi.org/10.1016/j.jastp.2004.03.022

Tóth, G., Sokolov, I. V., Gombosi, T. I., Chesney, D. R., Clauer, C. R., De Zeeuw, D. L., … Kóta, J. (2005). Space weather modeling framework: A new tool for the space science community. *Journal of Geophysical Research: Space Physics*, *110*(A12). Retrieved from `https://agupubs.onlinelibrary.wiley.com/doi/abs/10.1029/2005JA011126` doi: https://doi.org/10.1029/2005JA011126

Walker, R., Richard, R., Ogino, T., & Ashour-Abdalla, M. (1999). The response of the magnetotail to changes in the imf orientation: The magnetotail's long memory. *Physics and Chemistry of the Earth, Part C: Solar, Ter-*

restrial & Planetary Science, *24*(1), 221-227. Retrieved from `https://www.sciencedirect.com/science/article/pii/S1464191798000324` (International Symposium on Solar-Terrestrial Coupling Processes) doi: https://doi.org/10.1016/S1464-1917(98)00032-4

Wang, W., Wiltberger, M., Burns, A., Solomon, S., Killeen, T., Maruyama, N., & Lyon, J. (2004). Initial results from the coupled magnetosphere–ionosphere–thermosphere model: thermosphere–ionosphere responses. *Journal of Atmospheric and Solar-Terrestrial Physics*, *66*(15), 1425-1441. Retrieved from `https://www.sciencedirect.com/science/article/pii/S1364682604001506` (Towards an Integrated Model of the Space Weather System) doi: https://doi.org/10.1016/j.jastp.2004.04.008

Wang, Y., Zhuang, B., Hu, Q., Liu, R., Shen, C., & Chi, Y. (2016). On the twists of interplanetary magnetic flux ropes observed at 1 au. *Journal of Geophysical Research: Space Physics*, *121*(10), 9316-9339. Retrieved from `https://agupubs.onlinelibrary.wiley.com/doi/abs/10.1002/2016JA023075` doi: https://doi.org/10.1002/2016JA023075

Wanliss, J. A., & Showalter, K. M. (2006). High-resolution global storm index: Dst versus sym-h. *Journal of Geophysical Research: Space Physics*, *111*(A2). Retrieved from `https://agupubs.onlinelibrary.wiley.com/doi/abs/10.1029/2005JA011034` doi: https://doi.org/10.1029/2005JA011034

Welling, D. T., Love, J. J., Rigler, E. J., Oliveira, D. M., Komar, C. M., & Morley, S. K. (2021). Numerical simulations of the geospace response to the arrival of an idealized perfect interplanetary coronal mass ejection. *Space Weather*, *19*(2), e2020SW002489. Retrieved from `https://agupubs.onlinelibrary.wiley.com/doi/abs/10.1029/2020SW002489` (e2020SW002489 2020SW002489) doi: https://doi.org/10.1029/2020SW002489

Williams, D. J. (1983). The earth's ring current: Causes, generation, and decay. In J. G. Roederer (Ed.), *Progress in solar-terrestrial physics: Fifth international symposium held at ottawa, canada, may 1982* (pp. 223–234). Dordrecht: Springer Netherlands. Retrieved from `https://doi.org/10.1007/978-94-009-7096-0_17` doi: 10.1007/978-94-009-7096-0_17

Wiltberger, M., Wang, W., Burns, A., Solomon, S., Lyon, J., & Goodrich, C. (2004). Initial results from the coupled magnetosphere ionosphere thermosphere model: magnetospheric and ionospheric responses. *Journal of Atmospheric and Solar-Terrestrial Physics*, *66*(15), 1411-1423. Retrieved from `https://www.sciencedirect.com/science/article/pii/S136468260400149X` (Towards an Integrated Model of the Space Weather System) doi: https://doi.org/10.1016/j.jastp.2004.03.026

Yeates, A. R., Attrill, G. D. R., Nandy, D., Mackay, D. H., Martens, P. C. H., & van Ballegooijen, A. A. (2010, jan). COMPARISON OF a GLOBAL MAGNETIC EVOLUTION MODEL WITH OBSERVATIONS OF CORONAL MASS EJECTIONS. *The Astrophysical Journal*, *709*(2), 1238–1248. Retrieved from `https://doi.org/10.1088/0004-637x/709/2/1238` doi: 10.1088/0004-637x/709/2/1238

GEOPHYSICAL RESEARCH LETTERS

Supporting Information for ”A TIME-EFFICIENT, DATA DRIVEN MODELLING APPROACH TO PREDICT THE GEOMAGNETIC IMPACT OF CORONAL MASS EJECTIONS”

Souvik Roy[1], Dibyendu Nandy[1,2]

[1]Center of Excellence in Space Sciences India, Indian Institute of Science Education and Research Kolkata, Mohanpur 741246, India

[2]Department of Physical Sciences, Indian Institute of Science Education and Research Kolkata, Mohanpur 741246, India

Contents of this file

1. Text S1
2. Text S2
3. Figure S1
4. Figure S2
5. Table S1

Additional Supporting Information (Files uploaded separately)

1. Captions for Movies S1 to S4

Introduction The supporting information for the study is given here in terms of two text columns, one table, two figures and captions for four movies. We discuss the CESSI-

---

STORMI model setup and governing equations in supplementary text S1 and the Gold-Hoyle modelling in text S2. the choice of points in the equatorial plane to calculate the STORMI index is plotted in figure S1. The plot showing equatorial current distribution as a function of distance is depicted in figure S2. The quantitative evaluation of STORMI index is tabulated in table S1. Captions for the movies related to current distribution in the domain is given in corresponding sections. **Text S1.** Similar to CESSI SPIM (?, ?, ?), in CESSI-STORMI, we simulate a 3-dimentional domain developed in PLUTO (?, ?) architecture considering the interplanetary space, the planetary atmosphere and the solar wind as a single-fluid plasma. The interactions are governed by the adiabatic equation of state and the following set of resistive MHD equations.

$$\begin{aligned}
\frac{\partial \rho}{\partial t} + \nabla \cdot (\rho \mathbf{v}) &= 0 \\
\frac{\partial (\rho \mathbf{v})}{\partial t} + \nabla \cdot [\rho \mathbf{v}\mathbf{v} - \mathbf{B}\mathbf{B}] + \nabla \left(p + \frac{\mathbf{B}^2}{2} \right) &= \rho \mathbf{g} \\
\frac{\partial E_t}{\partial t} + \nabla \cdot \left[\left(\frac{\rho \mathbf{v}^2}{2} + \rho e + p \right) \mathbf{v} + c\mathbf{E} \times \mathbf{B} \right] &= \rho \mathbf{v} \cdot \mathbf{g} \\
\frac{\partial \mathbf{B}}{\partial t} + \nabla \times (c\mathbf{E}) &= 0.
\end{aligned}$$

The variables ρ, $\mathbf{v}$, $\mathbf{B}$, p, E_t denote the density, velocity, magnetic field, pressure and total energy density respectively. A factor of $\frac{1}{\sqrt{4\pi}}$ has been incorporated in the definition of $\mathbf{B}$ such that the total energy density E_t for an ideal gas can be written as,

$$E_t = \frac{p}{\gamma - 1} + \frac{\rho \mathbf{v}^2}{2} + \frac{\mathbf{B}^2}{2}$$

We use **g** as the acceleration experienced by the fluid due to the gravitational field of the planet in terms of body force vector. The electric field, **E**, having a convective and a resistive component, is written as,

$$c\mathbf{E} = -\mathbf{v} \times \mathbf{B} + \frac{\eta}{c}\mathbf{J}$$

Here $\mathbf{J} = c\nabla \times \mathbf{B}$ is the current density. We have neglected displacement currents in the system. Also, we consider a finite and isotropic magnetic diffusivity η which has a constant value ($10^{13}\, cm^2 s^{-1}$) throughout the simulation as the causal mechanism for non-ideal processes such as magnetic reconnections (?, ?, ?). To perform the integration, we have used HLL Riemann solver and linear interpolation in space, MINMOD limiter and 2$^{\text{nd}}$ order Runge-Kutta with "super-time-stepping" for temporal update. We impose the $\nabla \cdot \mathbf{B} = 0$ condition using the divergence-cleaning method, an approach based on the generalised formulation of the Lagrange multiplier (GLM). The left boundary of the domain is used as an inflow boundary for the solar wind and ICME whereas the other five boundaries are "outflow" boundaries for all the parameters.

The computational domain extends from $-205R_{\text{E}}$ to $205R_{\text{E}}$ in all three directions. A zone-wise static mesh refinement is implemented in the directions of the 3D Cartesian grid configuration such that the distance from the centre to $6R_{\text{E}}$ in all directions has been resolved with a grid-size of $0.3R_{\text{E}}$. From $6R_{\text{E}}$ to $25R_{\text{E}}$ the resolution is $0.5R_{\text{E}}$. The length of the grid-size increases to $1R_{\text{E}}$ between $25 \sim 50R_{\text{E}}$, then to $2R_{\text{E}}$ between $50 \sim 100R_{\text{E}}$ and finally to $3R_{\text{E}}$ as we move between $100 \sim 205R_{\text{E}}$.

Text S2. We model the flux rope using the Gold-Hoyle (GH) tube (?, ?) considering a axial symmetry of the topology. The twist is radially uniform and the magnetic field components, in cylindrical coordinates ($x = rcos\phi, y = rsin\phi, z = z$), are,

$$
\begin{aligned}
B_r &= 0,\\
B_\phi &= \tfrac{Tr}{1+T^2r^2}B_0,\\
B_z &= \tfrac{1}{1+T^2r^2}B_0.
\end{aligned}
$$

where B_0 is the magnitude of magnetic field at the axis of the flux rope and T is a constant representing the twist per unit length in the form of $\tau = \frac{T}{2\pi}$. The helicity of the flux rope in GH model is embedded in the right handed notion. For event 1, we get B_0 to be $-56\,$nT and τ to be $+3.8$ per astronomical unit (AU) using least squared fitting. The flux rope axis is inclined by an angle of -54^o to the ecliptic plane. On the other hand B_0 is $-19.5\,$nT and τ is -2.2 per AU for event 2, where the flux rope axis is parallel to the ecliptic plane.

Movie S1. The time evolution of the current distribution in the magnetosphere for event 1. The top left panel shows a view from the sun-side to a plane parallel to dipole axis. The top right panel shows a view from the west-side (dusk) to a plane normal to the equatorial plane. The middle right panel portrays a view from north pole to the equatorial plane. The time stamp is matched with the STORMI index calculation using a time slider in the bottom panel.

Table S1. Quantitative skill of the STORMI index in predicting the Dst and SYM-H indices for the events

Parameters		**Event 1**	**Event 2**
Maximum impact on	Dst SYM-H STORMI index	-422 nT at 20:00 UTC -490 nT at 18:17 UTC -523.9 nT at 17:03 UTC	-98 nT at 09:00 UTC -111 nT at 09:21 UTC -114.6 nT at 11:19 UTC
Pearson's r	for Dst	0.83 (99.99%)[a]	0.95 (99.99%)
	for SYM-H	0.88 (99.99%)	0.93 (99.99%)
Normalised RMS Error ($NRMSE$)[b]	for Dst	0.15	0.19
	for SYM-H	0.12	0.19
Prediction efficiency (PE)	for Dst	0.56	0.10
	for SYM-H	0.71	0.20

[a] The confidence level, calculated from the p-values using (1-p)×100%.

[b] Normalised over the range of the modelled data

Movie S2. A similar time evolution of the current distribution in the magnetosphere is as shown in Movie S1 but for event 2.

Movie S3. Time evolution of the cross-sectional θ-shaped current distribution of the magnetotail for event 1, as seen from far distant tail region. It is plotted in YZ-plane (STORMI coordinate) at a distance $60\,R_E$ from Earth. The a bottom time slider show the time stamp, which is matched with the STORMI index calculation.

Movie S4. A similar time evolution of the cross-sectional θ-shaped current distribution of the magnetotail is as shown in Movie S3 but for event 2.

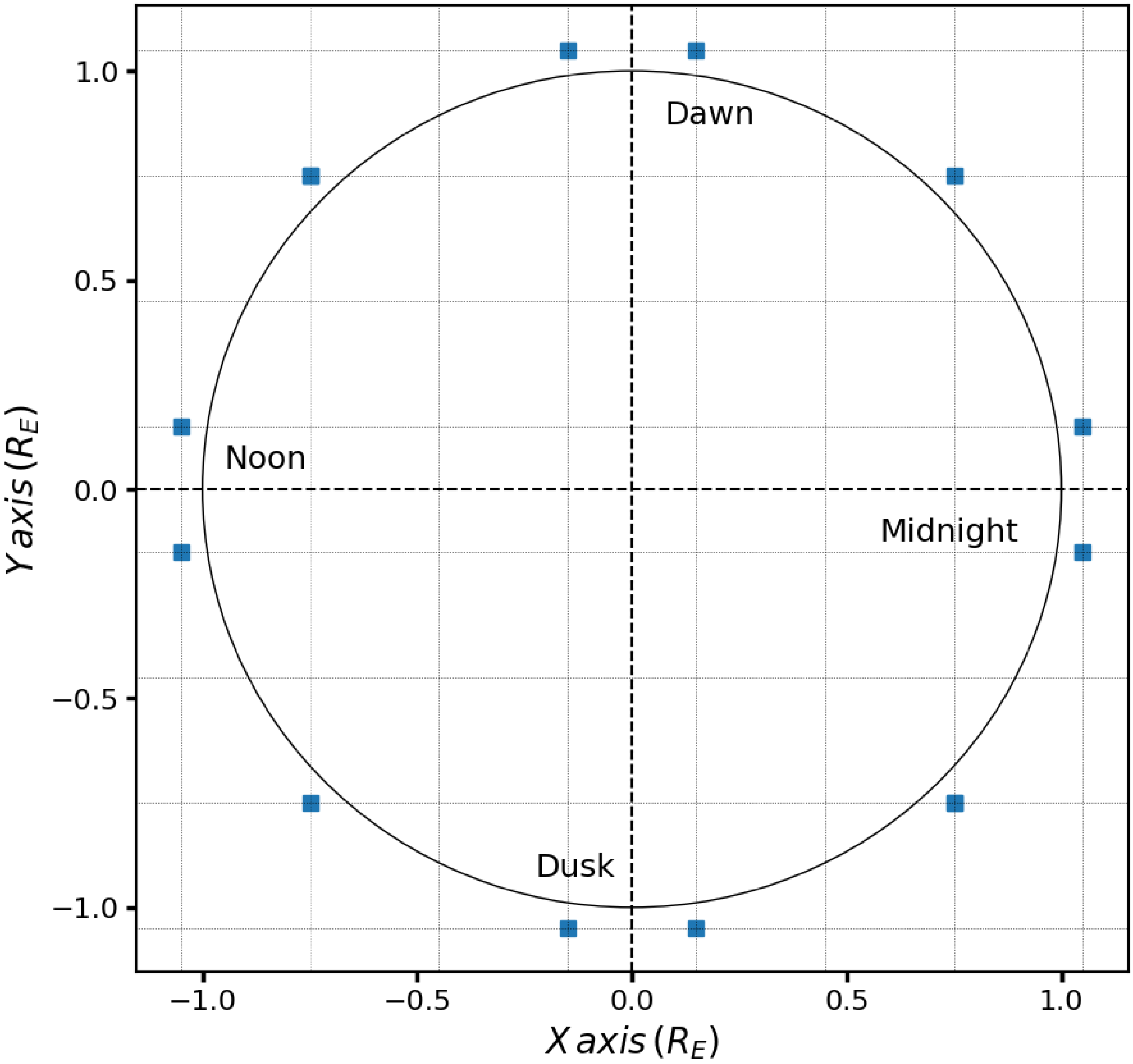

Figure S1. The figure shows the 2-dimensional distribution of the twelve points around the equator marked as blue squares. The equator is projected to the XY-plane in STORMI's coordinate system. The points are chosen as the nearest grid centres placed just outside the black circle that has a radius equal to that of Earth. The background cells corresponds to the near Earth grid resolution of STORMI where each corner represents a grid centre.

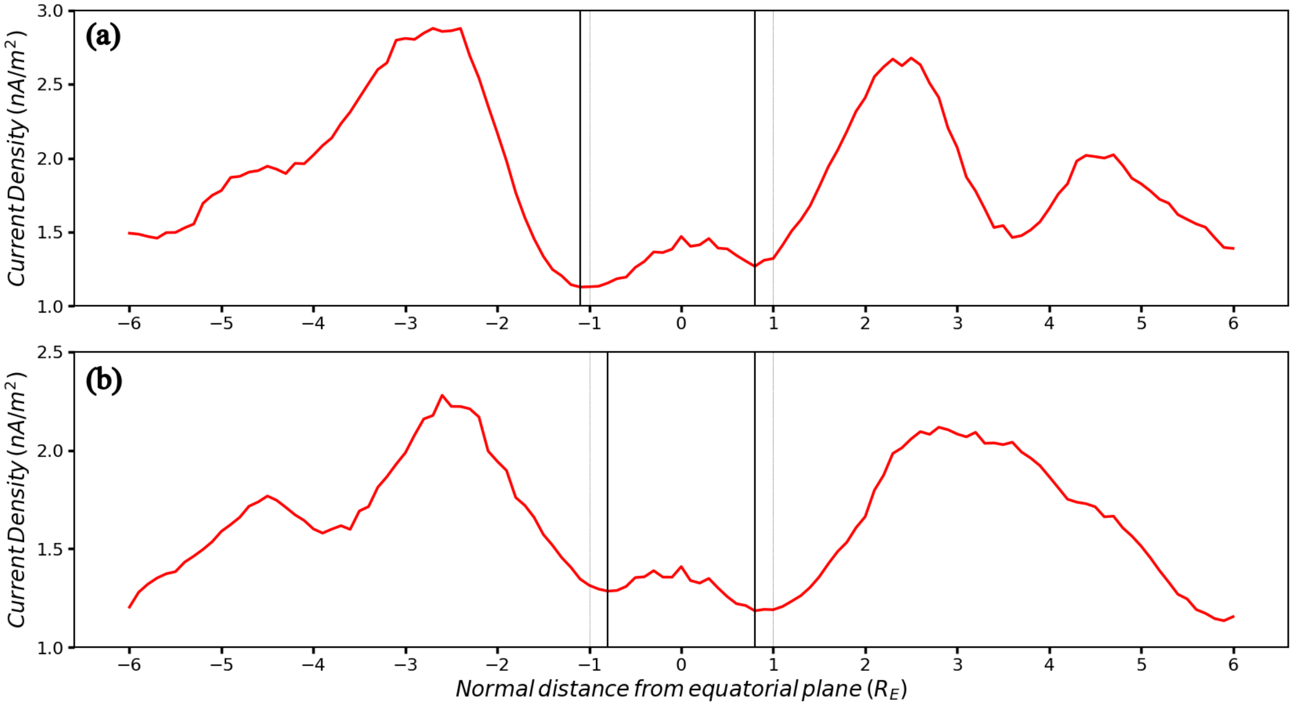

Figure S2. Panel **(a)** and **(b)** depict the distribution of time-averaged quiet time current density for event 1 and event 2 respectively. The current density is also averaged over circular plane surfaces parallel to equator and is plotted as a function of normal distance of corresponding planes from the equator. The tolerance in width of the circular planes are $0.1R_E$. The current shows a local maximum in the distribution near zero (equator). From the nearest local minimum values, we estimate the width of the distribution to be 1.9 R_E for event 1 and $1.6R_E$ for event 2 and calculate the STORMI index based on that.